

# Cu–Sn Alloy Nanoparticle-Modified Carbon Nanofibers for Dendrite-Free Zinc-Ion Batteries

Chang He, Qiao Jiang, Zhehan Yi, Jin Yu, Pinxiang Li, Shandong Tan, Ji Liang,\* and Feng Hou\*

Aqueous zinc-ion batteries (AZIBs) are currently highly promising rechargeable batteries offering affordable prices and high reliability. However, the uncontrolled expansion of zinc dendrites, hydrogen evolution reaction, and adverse reaction greatly affect their potential sustainable application. Herein, Cu–Sn nanoparticle alloy-modified carbon nanofibers (Cu/Sn–C) are constructed as a buffer interface region onto the zinc anode. The high density of zincophilic sites of the Cu/Sn–C contributes a homogeneous Zn deposition behavior, ameliorates potential separator penetration of zinc dendrites, and weakens corruptions and adverse reactions.

As a result, Cu/Sn–C exhibits a low zinc nucleation overpotential of 33.2 mV and dendrite-free zinc deposition. Besides, a symmetric cell with Cu/Sn–C@Zn anode exhibits outstanding cycling lifespan with over 3500 h at  $1 \text{ mA cm}^{-2}$  for  $1 \text{ mAh cm}^{-2}$ . Furthermore, Cu/Sn–C@Zn// $\text{Mn}_x\text{V}_2\text{O}_5$  full battery also achieves stable cycling at  $5 \text{ A g}^{-1}$ . This work provides a significant avenue for enhancing the reliability of the Zn anode, thereby facilitating the advancement of widespread applications for the next-generation AZIBs.

## 1. Introduction

Electrochemical energy storage technology, particularly in the form of batteries, has been extensively utilized across diverse fields. Among the promising candidates for energy storage options, aqueous zinc-ion batteries (AZIBs) have emerged as a leading option due to their low cost, high theoretical capacity ( $820 \text{ mAh g}^{-1}$ ), and low reduction potential ( $-0.76 \text{ V}$  vs SHE) of the Zn anode.<sup>[1,2]</sup> However, the commercial applications of AZIBs are hampered due to uncontrolled growth of zinc dendrites and harmful side reactions (corrosion, passivation of zinc, hydrogen evolution, and formation of by-products). These adverse issues result in low Coulombic efficiency (CE) of the battery, rapid capacity fading, and even battery failure.<sup>[3]</sup>

Fortunately, various effective strategies have been put forward to tackle these series of issues, including the engineering of 3D porous scaffolds,<sup>[4,5]</sup> surface modification,<sup>[6–9]</sup> electrolyte engineering,<sup>[10–13]</sup> and preparing artificial interface layers.<sup>[14–17]</sup> Among these solutions, building an interface layer upon the zinc anode is a universal and prospective strategy. The artificial interface layer shields  $\text{H}_2\text{O}/\text{O}_2$  by avoiding direct contact of zinc to the electrolyte, hence decreasing the generation of inert side reactions ( $\text{Zn}_4(\text{OH})_6\text{SO}_4 \cdot x\text{H}_2\text{O}$ ).<sup>[18]</sup> For instance, a matrix-filler hybrid interface is being developed to overcome the corrosion and

dendrite growth challenges in Zn metal anodes. As a result, symmetric cells display exceptional rate capability and high cycling capacity.<sup>[19]</sup> Nevertheless, with assistance from artificial interfacial layers, homogeneous deposition remains challenging because interfacial layers will also increase the roughness of the electrode surface morphology and slow down ion dynamics, resulting in high nucleation overpotentials and inevitable dendrite formation.<sup>[20]</sup> Therefore, it is a common strategy to introduce elements with high zinc affinity, such as Ag,<sup>[21]</sup> Zn–Sn alloy,<sup>[22]</sup> and Cu–Sn alloy<sup>[23]</sup> to decrease the nucleation site barriers. According to conventional heterogeneous nucleation theory, reducing the nucleation barrier toward more dense and homogeneous zinc formation.<sup>[24]</sup> However, despite the addition of zincophilic materials facilitating electrode surface morphology, their uneven distribution and aggregation will also lead to unequal  $\text{Zn}^{2+}$  fluxes and result in inconsistent zinc depositions. Generally, the most critical strategy to address the practical challenges is to design a uniform electric field and dendrite-free anode to achieve stable, highly effective ZIBs.

In this work, we innovatively constructed Cu–Sn nanoparticle alloy-modified carbon nanofibers (CNFs) (Cu/Sn–C) as a buffer interface region (BIR). The 3D carbon network structure of Cu/Sn–C has high conductivity and uniformly dispersed Cu–Sn nanoscale alloy with high zinc affinity. First, Cu/Sn–C effectively prevents direct contact of zinc to the electrolyte, hence decreasing the generation of  $\text{H}_2\text{O}$ -mediated parasitic adverse reactions. Moreover, the uniformly distributed Cu–Sn alloy with abundant zincophilic sites can not only regulate the Zn deposition behavior through Cu/Sn–C to suppress the forming of Zn dendrites but also minimize adverse reactions and extend the cycle lifespan. Herein, a symmetric cell with Cu/Sn–C@Zn anode exhibits superior reversibility and a stable lifetime with 3500 h at experimental conditions of  $1 \text{ mA cm}^{-2}$  and  $1 \text{ mAh cm}^{-2}$ . At high current density of  $5 \text{ mA cm}^{-2}$ , a long cycle life of 1500 h can also be achieved.

C. He, Q. Jiang, Z. Yi, J. Yu, P. Li, S. Tan, J. Liang, F. Hou  
Key Laboratory of Advanced Ceramics and Machining Technology of the  
Ministry of Education  
School of Materials Science and Engineering  
Tianjin University  
Tianjin 300350, China  
E-mail: liangji@tju.edu.cn  
houf@tju.edu.cn

 Supporting information for this article is available on the WWW under <https://doi.org/10.1002/batt.202500205>

The assembly of a full battery with  $Mn_xV_2O_5$  as the positive electrode has also achieved significant improvement in electrochemical performance. The modified CNFs designed in this study are a candidate material as a promising anode for stabilizing zinc ion negative electrodes.

## 2. Results and Discussion

The schematic diagram of the preparation process of Cu/Sn-C is depicted in Figure 1a. The preparation involves the dissolution of selected copper salts, tin salts, and polyvinylpyrrolidone (PVP) in suitable *N,N*-dimethylformamide (DMF) through electrospinning and high-temperature (600 °C) carbonization. The scanning electron microscopy (SEM) image of Cu/Sn-C in Figure 1b demonstrates that the prepared CNFs of Cu/Sn-C are uniform, presenting a width of  $\approx 200$  nm per CNF. The macroscopic optical image and bendable properties are shown in Figure S1, Supporting Information, and the SEM image in Figure S2, Supporting Information, characterizes the surface morphology of CNFs and Cu/Sn-C at low magnification. It can be seen that the entire carbon nanowire film is a porous 3D network structure composed of stable and continuous CNFs.

The morphology and elemental surface scan of the image in Figure 1c indicate that the elements C, N, Sn, and Cu exhibit a consistent distribution within in Cu/Sn-C, Cu-Sn alloy

distributed with uniform nanoparticles, and some of the particles with maximum diameters equal to  $\approx 10$  nm can be observed embedded in the Cu/Sn-C. As demonstrated in Figure 1d, the high-magnification transmission electron microscope (TEM) image provides a clearer visualization of the carbon fiber surface, which is distributed uniformly with a high density of particles. The lattice fringes of the  $Cu_3Sn$  (002) crystal plane can be observed from these particles, corresponding to an interplanar spacing of 0.22 nm.<sup>[25]</sup> In addition, the peak responses of Cu and Sn in the elemental line scan image of Figure S3, Supporting Information, can also substantiate the consistent dispersion of the Cu-Sn alloy within the CNFs.

The X-ray diffraction (XRD) pattern of Cu/Sn-C is shown in Figure 1e. No obvious peaks of samples are found before carbonization after electrostatic spinning, suggesting the absence of any significant crystalline structures. However, after carbonization at 600 °C, the presence of Cu-Sn alloy is observed, primarily consisting of  $Cu_3Sn$  and a minor amount of  $Cu_6Sn_5$ . This finding indicates that the carbonization process is the pivotal step in the formation of the highly crystalline Cu-Sn alloy nanoparticles. Furthermore, the Raman spectra detects the typical G peak and D peak of graphite of the CNFs and Cu/Sn-C (Figure S4, Supporting Information). In the context of a comparative analysis of the intensity ratio of G-band to D-band, it has been indicated that the results obtained are greater than 1, demonstrating that two materials exhibit a stable graphitic degree and electronic

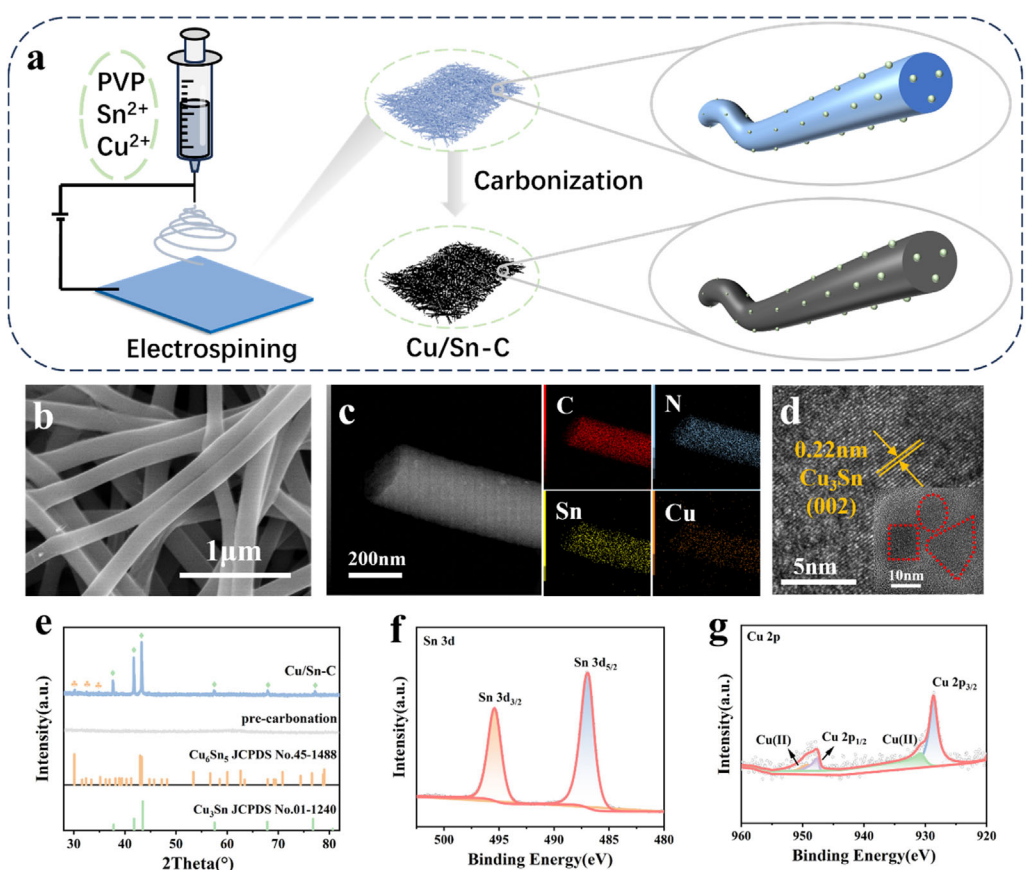


**Figure 1.** a) Synthesis schematic of Cu/Sn-C. b) Surface SEM of Cu/Sn-C. c) TEM image and corresponding elemental mapping images of Cu/Sn-C. d) High-resolution TEM images of Cu/Sn-C. e) XRD pattern of Cu/Sn-C. High-resolution XPS spectra of f) Sn 3d and g) Cu 2p of the Cu/Sn-C.

migration.<sup>[20]</sup> X-ray photoelectron spectroscopy (XPS) analysis can determine the chemical composition and valence states of surface elements of modified CNFs. The XPS full spectrum of Figure S5a, Supporting Information, shows the presence of C, Sn, Cu, N, and O elements. In the 3d spectrum of Sn in Figure 1f, two peaks of Sn<sup>0</sup> at 495.41 and 486.90 eV can be detected.<sup>[26]</sup> In the 2p spectrum of Cu in Figure 1g, two notable peaks are observed at 947.59 and 928.66 eV, corresponding to the detection of Cu<sup>0</sup>. And the two peaks of Cu(II) 2p can also be observed at 949.20 and 930.79 eV, which may be attributed to the fact that, in contrast to tin, which can be a fluid liquid at high temperatures, copper is in inadequate contact with H<sub>2</sub>, resulting in incomplete reduction. In the C 1s spectrum of Figure S5b, Supporting Information, three dominant peaks at 288.8, 285.93, and 284.8 eV can be observed, which are respectively related to the C—O, C=N, and C—C groups. The N 1s spectra in Figure S5c, Supporting Information, show peaks at 400.69, 399.39, and 398.44 eV corresponding to graphite-N, pyrrole-N, and pyridine-N, respectively.

The surface morphology of zinc deposited on the CNFs and Cu/Sn-C (Figure 2a,b) and the Zn foil protected by the CNFs BIR and Cu/Sn-C BIR (Figure 2c,d) is observed in SEM images after 50 cycles at a current density of 5 mA cm<sup>-2</sup> for 1 mAh cm<sup>-2</sup>. It was observed that the Zn morphology deposited on Cu/Sn-C still maintained a smooth and dense morphology. Moreover, the zinc affinity of Cu/Sn-C leads to the uniform deposition of zinc within the fiber network of Cu/Sn-C, without any dendritic spikes protruding (Figure 2b). However, in the case of CNFs, the Zn nuclei emerge randomly in the CNFs, these Zn nuclei have a tendency to become harmful dendrites after deposition of subsequent Zn<sup>2+</sup> owing to the locally distributed electric field (Figure 2a). Hence, the result is that the surface of Zn foil beside the CNFs layer is prone to be susceptible to the formation of Zn dendrites after

prolonged plating/stripping (Figure 2c). In contrast, the zinc foil beside Cu/Sn-C BIR maintains its smooth and flat characteristics, exhibiting a modulation of the Zn<sup>2+</sup> fluxes of the Cu<sub>3</sub>Sn (Figure 2d). The difference between two surfaces can be more intuitively understood by examining the in-situ optical microscope images of zinc deposition. Figure 2e,f shows the cross-sectional morphology of CNFs and Cu/Sn-C deposited at varying times (0–30 min) under a current density of 5 mA cm<sup>-2</sup>. It can be clearly seen that under the protection of CNFs, a substantial number of dense dendrites and by-products emerged during the zinc deposition process. Conversely, under the protection of Cu/Sn-C, the deposited zinc remained smooth and dense, devoid of any by-products accumulation, indicating that Cu/Sn-C possesses the capacity to dissolve dendrites.<sup>[27]</sup>

The wettability of the zinc anode surface is of crucial importance to the reversible plating/stripping and interfacial ion transfer of zinc. The static contact angle of CNFs in a 2 M ZnSO<sub>4</sub> electrolyte is 118.3° (Figure 3a). In contrast, the contact angle of Cu/Sn-C decreases to 58.7° (Figure 3b), thus showing a significant improvement in wettability. The contact angle between the electrolyte and Cu/Sn-C decreases significantly, corresponding to the better affinity between the electrolyte and the Cu/Sn-C interface. It is noteworthy that the improved contact angle wettability leads to a reduction in contact impedance at the electrolyte/electrode interface, thereby facilitating the uniform migration and deposition of zinc ions.<sup>[28,29]</sup>

To assess the corrosion resistance of the test electrode and its efficacy in suppressing side reactions, analyses are conducted of the composition and morphology of bare zinc and Zn foil protected by CNFs and Cu/Sn-C following immersion of the electrode in a 2 M ZnSO<sub>4</sub> electrolyte for 10 days. The XRD tests of bare zinc and Zn foil protected by CNF and Cu/Sn-C are shown

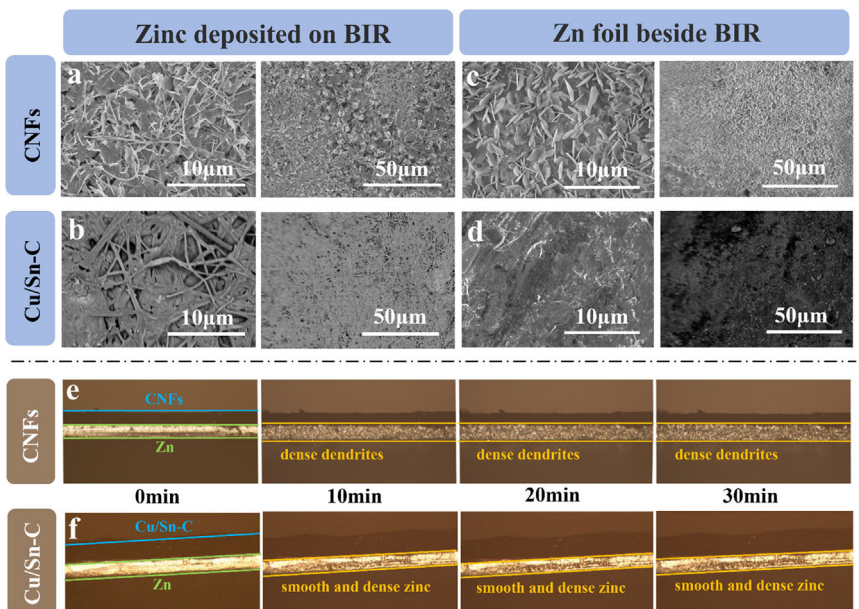


**Figure 2.** SEM images of zinc morphology on a) CNFs and b) Cu/Sn-C after 50 cycles at 5 mA cm<sup>-2</sup> for 1 mAh cm<sup>-2</sup>. SEM images of the zinc morphology of Zn foil stripped from c) CNFs and d) Cu/Sn-C after 50 cycles at 5 mA cm<sup>-2</sup> for 1 mAh cm<sup>-2</sup>. In situ optical microscopy images of e) CNFs and f) Cu/Sn-C at 5 mA cm<sup>-2</sup> for different times.

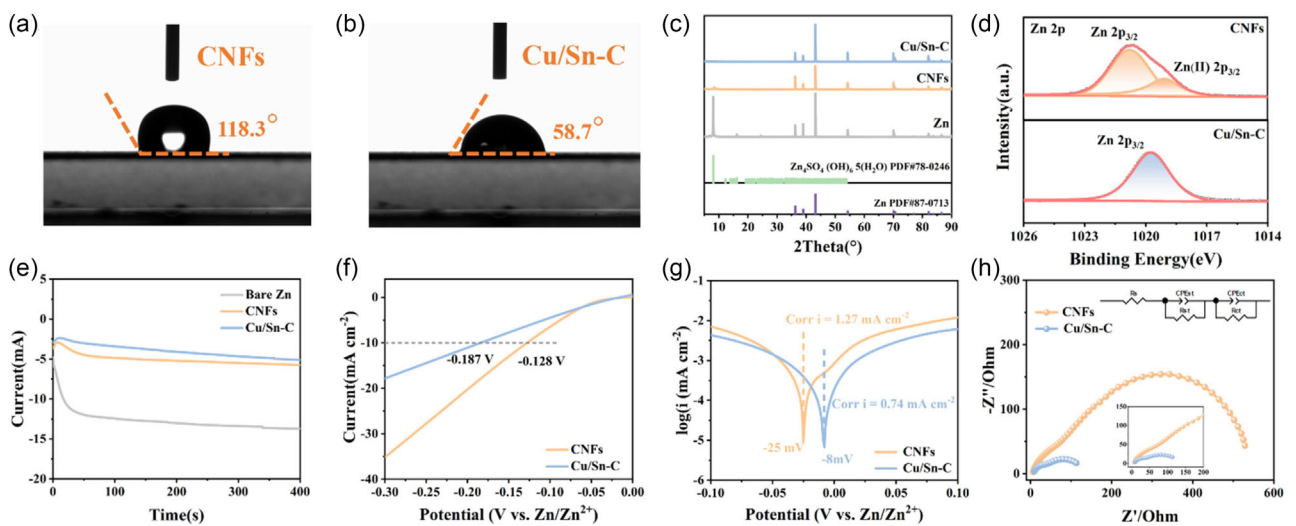


**Figure 3.** Contact angles of a) CNFs and b) Cu/Sn-C. c) XRD patterns of the electrodes after immersion in the electrolyte for 10 days. d) XPS spectra of Zn 2p<sub>3/2</sub> peak of CNFs and Cu/Sn-C deposited with 5 mAh cm<sup>-2</sup> of zinc. e) CA curves. f) Tafel curves and g) LSV curves of CNFs@Zn and Cu/Sn-C @Zn symmetrical batteries. h) Impedance spectra of Cu/Sn-C @Zn//Cu/Sn-C @Zn and CNFs@Zn//CNFs@Zn symmetrical cells.

in Figure 3c, a significant amount of by-products is observed on the bare zinc, indicating that zinc metal is unable to exist stably with the electrolyte. In contrast, the characteristic diffraction peak intensity of Zn by-products is significantly reduced under the protection of CNFs and Cu/Sn-C. This is due to the interface layer's ability to prevent direct contact between zinc and electrolyte, thereby shielding H<sub>2</sub>O/O<sub>2</sub> and reducing the formation of inert side reactions such as zinc hydroxide sulfate hydrate (Zn<sub>4</sub>SO<sub>4</sub>(OH)<sub>6</sub>·5H<sub>2</sub>O). The Zn foil protected by Cu/Sn-C shows no significant change in composition, indicating that the Cu/Sn-C greatly inhibits corrosion. The SEM images and corresponding energy dispersive spectrometer (EDS) maps of the three electrodes after immersion are presented in Figure S6, Supporting Information. On the exposed surface of Zn, randomly oriented hexagonal flakes of different sizes can be found. In contrast, with the protection of CNFs, dendrites are significantly reduced, the most satisfying is that with the protection of Cu/Sn-C, Zn foil maintains its original state and almost no by-products are detected. Similarly, after deposition with 5 mAh cm<sup>-2</sup> of zinc, CNFs emits a Zn(II) 2p<sub>3/2</sub> peak, and the Zn<sup>0</sup> 2p<sub>3/2</sub> peak of CNFs shows a higher binding energy than Cu/Sn-C (Figure 3d), suggesting that less hydrogen evolution reaction (HER) by-products (Zn<sub>4</sub>(OH)<sub>6</sub>SO<sub>4</sub>·xH<sub>2</sub>O) are generated on the Cu/Sn-C.<sup>[30]</sup>

Chronoamperometry (CA) testing is conducted at -150 mV to analyze the migration and deposition behavior of Zn<sup>2+</sup>, as shown in Figure 3e. The current of bare Zn is the highest and continues to rise within 400 s, exhibiting disordered 2D diffusion behavior. This diffusion behavior indicates irregular nucleation of Zn caused by the uneven deposition of Zn<sup>2+</sup>. Conversely, the current of the CNFs@Zn and Cu/Sn-C@Zn is significantly reduced due to the guiding effect of the interface layer on Zn deposition, with the Cu/Sn-C@Zn exhibiting a minimal current. This phenomenon can be attributed to the presence of alloys with high zinc affinity, which function as nucleation sites for Zn<sup>2+</sup>. This facilitates uniform deposition of Zn<sup>2+</sup>, thereby preventing concentrated diffusion and deposition.<sup>[31]</sup>

Tafel curves are implemented for Cu/Sn-C@Zn and CNFs@Zn symmetrical batteries to evaluate the corrosion performance. As depicted in Figure 3f, the corrosion current of the Cu/Sn-C@Zn symmetrical batteries decreases from 1.27 to 0.74 mA cm<sup>-2</sup> compared to CNFs@Zn. In contrast, the Cu/Sn-C@Zn manifests a higher corrosion potential, thereby demonstrating its capacity to offer enhanced corrosion resistance. The linear sweep voltammetry (LSV) curve in Figure 3g shows that at a current of -10 mA cm<sup>-2</sup>, the overpotential of Cu/Sn-C@Zn is -0.184 V, which demonstrates a higher HER overpotential than the CNFs@Zn (-0.128 V), the higher HER overpotential of Cu/Sn-C@Zn indicating the effective mitigation of the hydrogen evolution reaction.

In addition, the electrochemical impedance spectroscopy (EIS) in Figure 3h shows that the Cu/Sn-C@Zn exhibits a reduced charge transfer resistance in comparison with CNFs@Zn, suggesting that ions transfer more rapidly at the Cu/Sn-C, thereby facilitating the uniform and stable electroplating stripping of Zn<sup>2+</sup>.

As we all known, constructing the affinity between the Zn<sup>2+</sup> and the electrode is advantageous in a number of ways. First, it has been demonstrated to reduce the interfacial free energy of the zinc substrate. Moreover, this approach has been shown to effectively promote a uniform Zn<sup>2+</sup> stripping/plating behavior and finally optimize the electrochemical performances of the anode.<sup>[32]</sup> To acquire a deeper understanding of the mechanisms involved in the affinity between the Cu<sub>3</sub>Sn and zinc and zinc deposition regulation of Cu/Sn-C at the atomic level, we have conducted density functional theory (DFT) calculations of adsorption energy. According to the calculations, the adsorption energies of Zn<sup>2+</sup> on carbon, Zn (002) and Cu<sub>3</sub>Sn (002) substrates are -0.25, -0.39 and -1.52 eV, respectively (Figure 4a). This finding indicates that Cu<sub>3</sub>Sn exhibits the strongest binding affinity for Zn compared to carbon and pure Zn.<sup>[33,34]</sup> Furthermore, DFT-based interfacial charge-density models of Carbon, Zn(002), and Cu<sub>3</sub>Sn(002) with Zn atom adsorption are summarized in Figure 4b. The results of local charge density

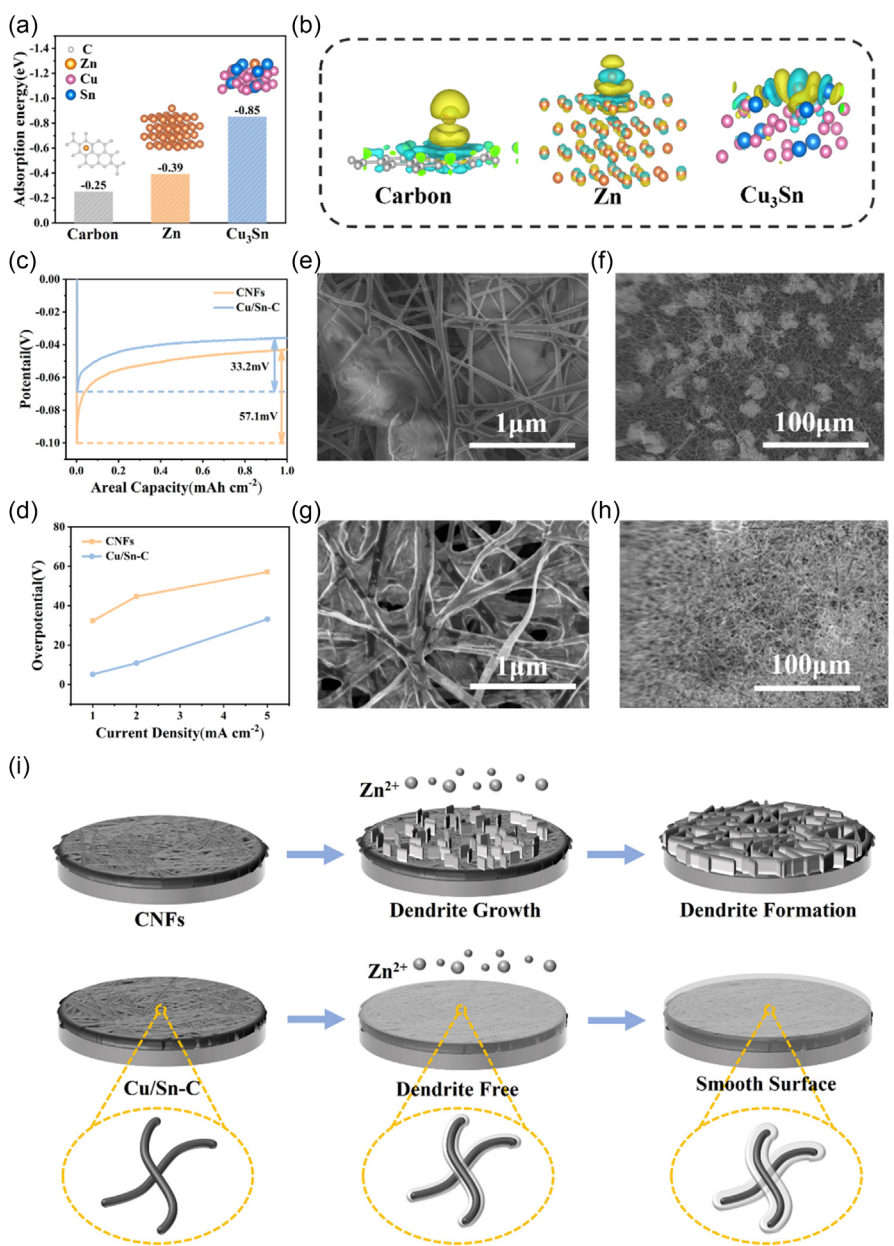


**Figure 4.** a) Summary of the calculated adsorption energies and calculation model of Zn atom absorbed on Carbon, Zn (002), and Cu<sub>3</sub>Sn (002) facets. b) Interfacial charge density models of Carbon, Zn, and Cu<sub>3</sub>Sn with Zn atom adsorption. c) Nucleation overpotential at 5 mA cm<sup>-2</sup>. d) Nucleation overpotential at different current densities. SEM images of zinc deposition with a capacity of 1 mAh cm<sup>-2</sup> deposited on e,f) CNPs and g,h) Cu/Sn-C at 1 mA cm<sup>-2</sup>. i) Schematic illustration of Zn deposition process of CNPs and Cu/Sn-C.

confirm that Cu<sub>3</sub>Sn and Zn atoms indicate the strongest electronic interaction and the largest polarization between the interface. The strong affinity between Cu<sub>3</sub>Sn and Zn atoms demonstrates that Cu<sub>3</sub>Sn introduced into CNPs shows strong zincophilicity and can mitigate the aggregation of Zn dendrite.

More evidence is confirmed in Figure 4c, the deposition curve of zinc indicates that the nucleation overpotential of Cu/Sn-C at a current density of 5 mA cm<sup>-2</sup> is 34.1 mV, which is much lower than the high nucleation overpotential of 68.4 mV on CNPs. Similarly, Figure 4d provides a comprehensive overview of the nucleation overpotentials of Cu/Sn-C and CNPs at a range of densities (1, 2, and 5 mA cm<sup>-2</sup>). The diminished nucleation

overpotential of Cu/Sn-C further suggests that the introduced Cu-Sn alloy possesses high zinc affinity, thereby providing more nucleation sites for zinc.

In order to visually observe the regulatory effect of Cu/Sn-C on the nucleation and deposition of Zn, the morphological changes of Zn after deposition were shown through SEM. Figure 4e,f and S7, Supporting Information, illustrate the surface morphology of zinc with a capacity of 1 and 5 mAh cm<sup>-2</sup> deposited on CNPs layer and Cu/Sn-C BIR at a current density of 1 mA cm<sup>-2</sup>. It is evident from the images that the surface of the CNPs layer exhibits distinctive plate-like structures of Zn, accompanied by uneven deposition, which can potentially

induce localized current concentration within the battery. This, in turn, can lead to the formation of dendrites and the occurrence of irreversible short circuits. As illustrated in Figure 4g,h, the zinc deposited on the Cu/Sn-C BIR exhibits a smooth and dense character. This phenomenon can be attributed to the high density of zincophilic Cu-Sn alloys distributed on the CNFs. Consequently,  $Zn^{2+}$  tends to deposit along the periphery of carbon fibers. This arrangement maintains the network structure of the uniform electric field, thereby facilitating the uniform deposition of  $Zn^{2+}$ .

To conclude, these evidences show that  $Cu_3Sn$  exhibits a significantly higher zinc affinity binding site than carbon. This finding indicates that  $Cu_3Sn$  can provide a lower deposition energy barrier, thereby promoting the adsorption of Zn atoms on the surface of Cu/Sn-C. Consequently, this process drives the heterogeneous nucleation of Zn. Therefore, it can be concluded that the high density of  $Cu_3Sn$  doped in CNFs is conducive to the uniform growth and formation of Zn along the periphery of CNFs. Thus, the process of Zn nucleation and

deposition of CNFs and Cu/Sn-C interfacial layers can be depicted, which is illustrated schematically in Figure 4i. The following points summarize the advantages of the Cu/Sn-C in restraining Zn dendrite growth: First, calculations of adsorption energy and electrochemical results indicate that the Cu/Sn-C interface exhibits a low overpotential for nucleation and an enhanced ability to inhibit HER by-products, thereby modulating Zn deposition behavior and mitigating the formation of Zn dendrites. Additionally, the conductive network of Cu/Sn-C facilitates uniform electron transfer, thereby ensuring a consistent electric field distribution.

In the cyclic voltammetry (CV) analysis of Figure 5a, Cu/Sn-C@Zn exhibits a larger response current and narrower potential separation, indicating that the modified sample can more effectively induce zinc nucleation with faster reaction kinetics.<sup>[35]</sup> Moreover, Cu/Sn-C@Zn symmetric batteries exhibit lower overpotentials in comparison with CNFs@Zn symmetric batteries at varying current densities (1, 2, 5, 8, 10 mA cm<sup>-2</sup>; Figure 5c),

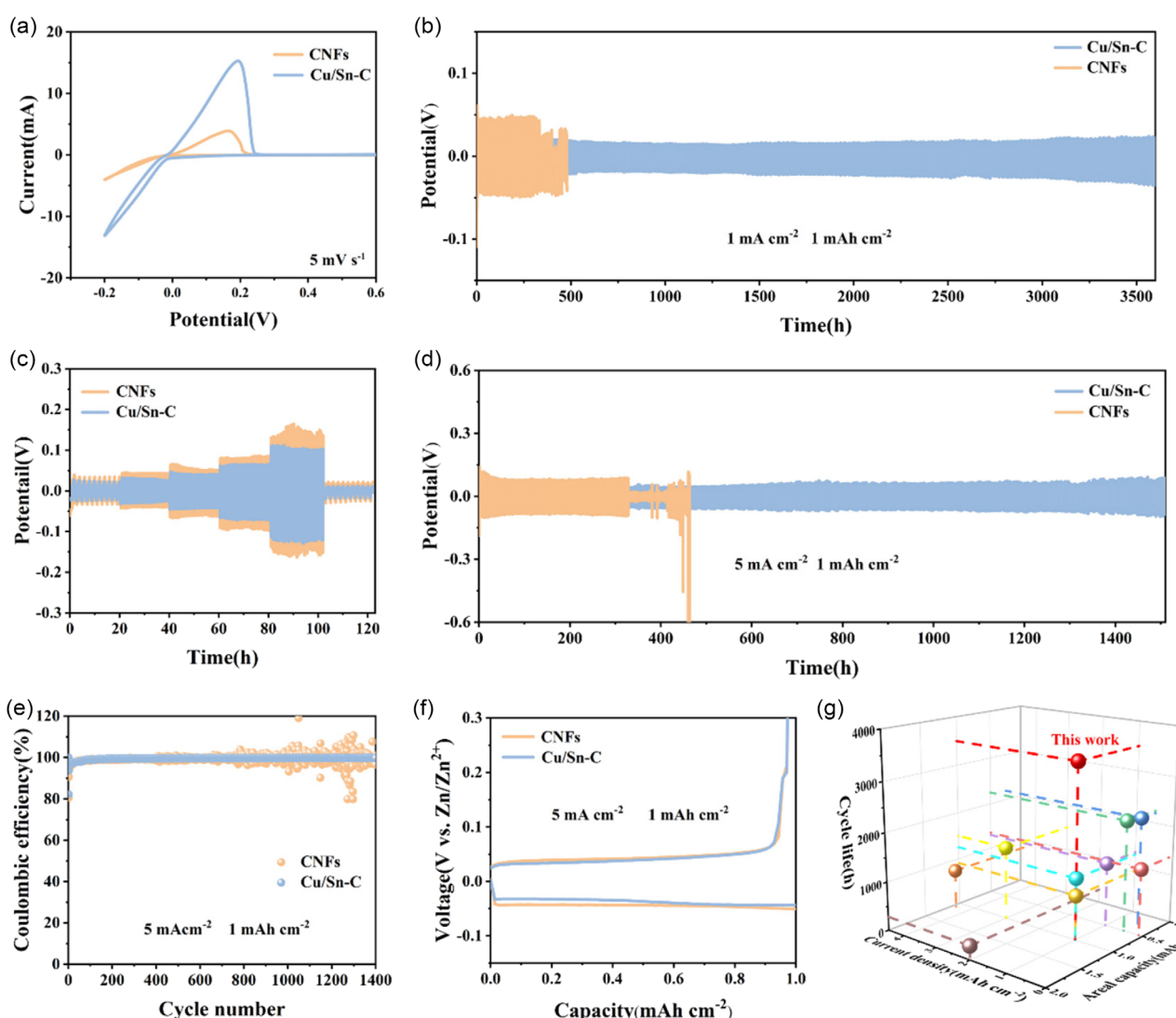


**Figure 5.** a) CV curves. b) Cycling performance of Cu/Sn-C and CNFs symmetric cells at 1 mA cm<sup>-2</sup> for 1 mAh cm<sup>-2</sup>. c) Rate performance of Cu/Sn-C and CNFs symmetric cell. d) Cycling performance of Cu/Sn-C and CNFs symmetric cells at 5 mA cm<sup>-2</sup> for 1 mAh cm<sup>-2</sup>. e,f) CE and voltage profiles of Cu/Sn-C and CNFs. g) Comparison of long-term cycling performance of this work and other previous work at different current densities and areal capacities.

revealing the exceptional rate performance of Cu/Sn-C@Zn symmetric batteries.

Next, symmetric batteries are assembled to assess their cycling stability. Under the testing conditions of a current density of  $1 \text{ mA cm}^{-2}$  and a surface area of  $1.0 \text{ mAh cm}^{-2}$ , Cu/Sn-C@Zn symmetric batteries can achieve a long-term cycle lifetime of 3500 h. In contrast, CNFs@Zn symmetric batteries tend to short-circuit after 400 h (Figure 5b). When the current density is increased to  $5 \text{ mA cm}^{-2}$  (Figure 5d) and even  $10 \text{ mA cm}^{-2}$  (Figure S8, Supporting Information), the Cu/Sn-C@Zn symmetric battery retains a cycle life of more than 1500 and 1200 h, respectively. Even at  $5 \text{ mA cm}^{-2}$  for  $5 \text{ mAh cm}^{-2}$ , the Cu/Sn-C@Zn symmetric batteries display a steady operation over 540 h. In comparison, the CNFs@Zn symmetric cells only deliver lifespans of 300, 60, and 50 h under the aforementioned test conditions, respectively. The sudden failure of CNFs@Zn symmetric batteries is mainly attributed to the uncontrolled growth of Zn dendrites and the adverse reactions generated.

Assemble a half cell and measure CE to study the reversibility and stability of Cu/Sn-C anode, as depicted in Figure 5e and S9, Supporting Information. Both CNFs and Cu/Sn-C can be stably cycled for 1000 cycles at  $1 \text{ mA cm}^{-2}$  and  $1 \text{ mAh cm}^{-2}$  test conditions (Figure S9a, Supporting Information), and the voltage hysteresis corresponding to Cu/Sn-C is much lower than that of CNFs (Figure S9b, Supporting Information). However, under the test conditions of a current density of  $5 \text{ mA cm}^{-2}$  and  $1 \text{ mAh cm}^{-2}$ , for CNFs, the assembled cell rapidly fails after 400 cycles, and the CE rate curve fluctuates and becomes unstable. Conversely, the Cu/Sn-C anode exhibits stable galvanizing/stripping behavior, with an average CE of 99.6% after 1000 cycles, thereby demonstrating its efficacy in enhancing the cycling

stability of batteries. The underlying mechanism is attributed to the steady electric fields of Cu/Sn-C, which facilitate the diminution of localized current densities during cycling.<sup>[36]</sup> Additionally, the Cu-Sn alloy functions as a deposition site, guiding the uniform deposition of zinc. With regard to the platform overpotential (Figure 5f), at a current density of  $5 \text{ mA cm}^{-2}$ , the corresponding voltage hysteresis of the Cu/Sn-C is only 64.7 mV, which is lower than that of CNFs (80.5 mV). This demonstrates the enhanced reaction kinetics for Cu/Sn-C.

Furthermore, the comparison between Figure 5g and Table S1, Supporting Information, shows that under the testing parameters of a current density of  $1 \text{ mA cm}^{-2}$  for  $1.0 \text{ mAh cm}^{-2}$ , the ability to maintain a long-term consistent lifespan is ahead of most reported Zn anodes.

To further demonstrate the viability of Cu/Sn-C@Zn anode in practical applications, a full battery (represented as Cu/Sn-C@Zn//MVO) is assembled utilizing  $\text{Mn}_x\text{V}_2\text{O}_5$  (MVO) as the cathode. The TEM image of MVO is shown in Figure S10, Supporting Information. We compared its performance with the CNFs@Zn//MVO battery, which uses CNFs as the anode.<sup>[37]</sup> In the CV curve (Figure 6a), similar shapes and redox peaks are detected in Cu/Sn-C@Zn//MVO and CNFs@Zn//MVO batteries. In contrast, Cu/Sn-C@Zn//MVO battery demonstrates reduced voltage polarization on the CV curve, indicating that Cu/Sn-C@Zn anode can improve reaction kinetics. A comparison of the rate capability of Cu/Sn-C@Zn//MVO and CNFs@Zn//MVO at a range of current densities is depicted in Figure 6b. The Cu/Sn-C@Zn//MVO battery exhibits higher capacity, indicating improved cycling and rate performance of the Cu/Sn-C@Zn assembled full battery. The validity of this result is further confirmed by capacity–voltage curves (Figure 6c and S11, Supporting Information).

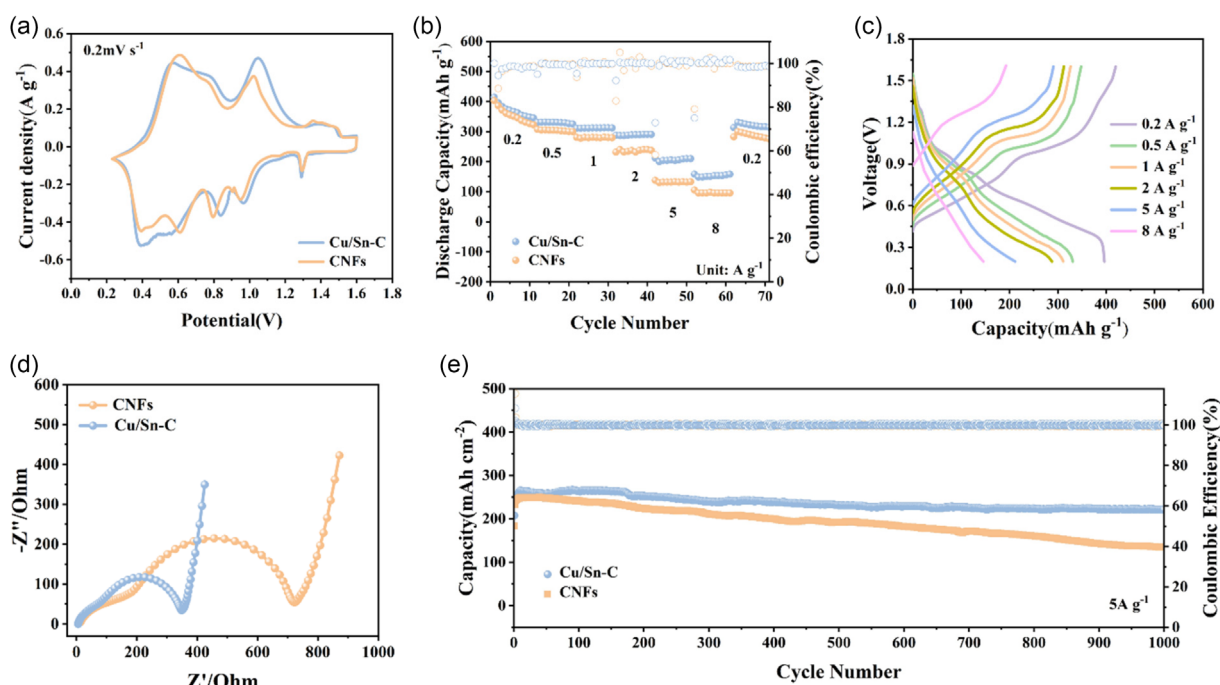


**Figure 6.** a) CV curves of Cu/Sn-C @Zn//MVO and CNFs@Zn//MVO batteries at scan rates of  $0.2 \text{ mV s}^{-1}$ . b) Rate performances of Cu/Sn-C @Zn//MVO and CNFs@Zn//MVO batteries under different current densities. c) Capacity–voltage profiles of Cu/Sn-C @Zn//MVO at different current densities. d) EIS curves of Cu/Sn-C @Zn//MVO and CNFs@Zn//MVO batteries. e) Cycling performance curves of full batteries at  $5 \text{ A g}^{-1}$ .

Furthermore, the EIS results of Cu/Sn–C@Zn//MVO battery (Figure 6d) indicate a reduction in the charge transfer resistance, revealing that the reaction kinetics of Cu/Sn–C are faster. More importantly, following 1000 cycles at 5 A g<sup>-1</sup>, the capacity of the Cu/Sn–C@Zn//MVO battery remains at 221.42 mAh g<sup>-1</sup> with an impressive capacity retention of around 90.2%. By contrast, the battery of CNFs@Zn//MVO can only remain at around 135.48 mAh g<sup>-1</sup> with a disappointing capacity retention around 55.15% (Figure 6e).

### 3. Conclusion

In conclusion, we successfully fabricated Cu/Sn–C with abundant zincophilic sites by the electrospinning method as BIR to stabilize the zinc anode. High density dispersed Cu–Sn alloy with high zinc affinity was found to modulate the zinc deposition process to suppress the creation of Zn dendrites, as well as suppressing adverse reactions, thus extending the cycle life. The symmetry cells of the Cu/Sn–C@Zn anode have been shown to achieve a long cycle life of 3500 h at 1 mA cm<sup>-2</sup>, and excellent rate performance has been demonstrated. Following 1000 cycles, the Cu/Sn–C@Zn//MVO battery achieves higher reversible capacity in comparison with the CNFs@Zn//MVO full battery. This work outlines an innovative approach to the stabilization of zinc ion anodes, thereby facilitating the advancement of AZIBs toward widespread applications.

## 4. Experimental Section

### Materials Synthesis: Raw Material

Tin (II) chloride dihydrate ( $\text{SnCl}_2 \cdot 2\text{H}_2\text{O}$ , Heowns), cupric chloride dihydrate ( $\text{CuCl}_2 \cdot 2\text{H}_2\text{O}$ , Aladdin), PVP (Sigma), DMF (Kermel), and Zn foils (purity 99.99%). The water used in this research was deionized water. The separator was GF/F glass fiber filters purchased from Whatman, and the components of the CR-2032 coin-type cell were purchased from Carnd.

### Materials Synthesis: Synthesis of the Cu/Sn–C and CNFs

In a typical process, 0.6 g  $\text{SnCl}_2 \cdot 2\text{H}_2\text{O}$  was added in 10 mL DMF with vigorous stirring for 30 min. Then, 1.4 g  $\text{CuCl}_2 \cdot 2\text{H}_2\text{O}$  was added with continuous 30 min stirring. Afterward, 2 g PVP was dissolved to the mixture, followed by vigorous stirring for 14 h. The obtained suspension was then poured into a syringe during the electrospinning process. The voltage during electrostatic spinning was set to 18 kV, and the feed rate of the needle was fixed at 0.8 mL h<sup>-1</sup>. Then, the membranes were calcinated at 260 °C with 1 °C min<sup>-1</sup> for 2 h and then at 600 °C with 2 °C min<sup>-1</sup> in H<sub>2</sub>/Ar atmosphere for 2 h. The obtained product was denoted Cu/Sn–C. For comparison, CNFs were also synthesized in the absence of  $\text{SnCl}_2 \cdot 2\text{H}_2\text{O}$  and  $\text{CuCl}_2 \cdot 2\text{H}_2\text{O}$  in the precursor solution and under the same conditions as previously outlined.

### Materials Synthesis: Synthesis of the Anode

The Cu/Sn–C@Zn and CNFs@Zn were made by pressing Cu/Sn–C and CNFs onto Zn foil (0.1 mm), subsequently forming pouched them to 12 mm discs.

### Materials Synthesis: Synthesis of $\text{Mn}_{0.25}\text{V}_2\text{O}_5$

In a typical synthesis process, 0.273 g commercial  $\text{V}_2\text{O}_5$  powder was added to 35 mL H<sub>2</sub>O with vigorous stirring. After 30 min, Mn ( $\text{CH}_3\text{COO}$ )<sub>2</sub>·4H<sub>2</sub>O was added into the turbid mixture, followed by the dropwise addition of 30% H<sub>2</sub>O<sub>2</sub> (2 mL) which was added to the solution dropwise. Concurrently, CH<sub>3</sub>COOH (2.2 mL) was added simultaneously with the pH 3–4. Following stirring for 2 h, the solution was hydrothermally treated at 210 °C for 48 h. Subsequently, the sediment was collected and washed with H<sub>2</sub>O and ethanol 3 times. Then, the powders were dried under vacuum at 60 °C for 12 h to obtain pure  $\text{Mn}_{0.25}\text{V}_2\text{O}_5$ .<sup>[37]</sup>

### Materials Synthesis: Synthesis of Cathode

In a typical synthesis process,  $\text{Mn}_{0.25}\text{V}_2\text{O}_5$  powder, super P, and polytetrafluoroethylene were mixed (7:2:1 mass ratio) in ethanol. Then, the mixture was well mixed to make a smooth liquid. This liquid was put on a stainless steel foil and vacuum dried at 80 °C without air.

### Materials Synthesis: Assembly of Coin-Type Cell

Electrodes were pouched to 12 mm discs. With Whatman GF/F as the separator ( $\Phi = 16$  mm) and 115  $\mu\text{L}$  2.5 M ZnSO<sub>4</sub> as an aqueous electrolyte, the cell was rested for 2 h before testing.

### Characterization of Materials

Field-emission SEM was performed using Hitachi S-4800 SEM with EDS for element distribution. TEM and selected area electron diffraction were conducted using JEOL JEM-F200 TEM with 200 kV operating voltage, and EDS maps were obtained at 15 kV with 80 mm<sup>2</sup> × 80 mm<sup>2</sup> Oxford X-Max detector. XRD was conducted using Bruker, D8 advanced diffractometer (Cu K $\alpha$  radiation,  $\lambda = 0.154$  nm, and the scan rate was 0.1 s for each step and the increment was 0.02°) at room temperature. XPS was conducted using Thermo Scientific ESCALAB 250Xi with a monochromatized Al K $\alpha$  ( $h\nu = 1486.6$  eV) X-ray source. The accelerating voltage was 15 kV, the current was 15 mA, and the chamber had a base pressure of  $5 \times 10^{-9}$  torr.

### Electrochemical Measurements

The Zn electrodeposition performances of Cu/Sn–C and CNFs were tested on the Neware battery test system in Zn//Cu/Sn–C and Zn//CNFs coin-type electrochemical cells (CR2032) at room temperature. For the investigation of CE, Zn was the counter electrode; Cu/Sn–C, CNFs and bare Cu foil were the working electrodes. The cut-off potential was 0.5 V during the Zn stripping process. CA, Tafel curves, LSV, EIS, and CV tests were conducted using a CHI660e electrochemical workstation. Symmetric cell performance tests were conducted under the conditions of 1, 2, 5, and 10 mA cm<sup>-2</sup> for 1 mAh cm<sup>-2</sup> on the Neware battery test system. For the full cell testing, current densities of 0.2, 0.5, 1, 2, 5, 8, and 0.2 A g<sup>-1</sup> were used for the rate of multiplication performance testing, and current densities of 5 A g<sup>-1</sup> were used for long-cycle performance testing, all with voltage intervals of 0.2–1.6 V.

### Computational Methods

All the computational tasks were accomplished with the of DFT, as implemented by the Vienna Ab Initio Simulation Package.<sup>[38]</sup> For all the calculations, the Perdew–Burke–Ernzerhof<sup>[39]</sup> approach was utilized on the basis of periodically repeated slab models. To mitigate

the effects of interactions between neighboring images, a vacuum layer exceeding 15 Å was incorporated. The energy cutoff value for the plane wave basis was set at 450 eV, while the convergence criteria for residual forces and total energies were specified as 0.03 eV Å<sup>-1</sup> and 1 × 10<sup>-6</sup> eV, respectively. To rectify the van der Waals interaction, Grimme's zero damping DFT-D3 dispersion correction scheme was adopted. A uniformly G-centered 3 × 3 × 1 k-point mesh and Methfessel–Paxton electronic smearing were employed for integration within the Brillouin zone during geometric optimization.

## Acknowledgements

This work was supported by the National Natural Science Foundation of China (grant nos. 22179093 and 21905202).

## Conflict of Interest

The authors declare no conflict of interest.

## Data Availability Statement

The data that support the findings of this study are available from the corresponding author upon reasonable request.

**Keywords:** alloys • aqueous zinc-ion batteries • carbon nanofibers • density functional calculations • Zn dendrite

- [1] X. J. Chen, W. Li, D. Reed, X. L. Li, X. B. Liu, *Electrochim. Energy Rev.* **2023**, *6*, 89.
- [2] Y. F. Li, D. Y. Zhao, J. J. Cheng, Y. Lei, Z. S. Zhang, W. M. Zhang, Q. C. Zhu, *Chem. Eng. J.* **2023**, *452*, 10.
- [3] F. Y. Liu, Y. Q. Zhang, H. Liu, S. X. Zhang, J. Y. Yang, Z. Li, Y. H. Huang, Y. Ren, *ACS Nano* **2024**, *18*, 16063.
- [4] S. N. Yang, Y. T. Li, H. X. Du, Y. Q. Liu, Y. H. Xiang, L. Z. Xiong, X. M. Wu, X. W. Wu, *ACS Sustainable Chem. Eng.* **2022**, *10*, 12630.
- [5] Q. Zhang, J. Y. Luan, L. Fu, S. G. Wu, Y. G. Tang, X. B. Ji, H. Y. Wang, *Angew. Chem., Int. Ed.* **2019**, *58*, 15841.
- [6] Q. Li, A. Chen, D. H. Wang, Y. W. Zhao, X. Q. Wang, X. Jin, B. Xiong, C. Y. Zhi, *Nat. Commun.* **2022**, *13*, 9.
- [7] J. Cao, X. Wang, S. S. Qian, D. D. Zhang, D. Luo, L. L. Zhang, J. Q. Qin, X. Y. Zhang, X. L. Yang, J. Lu, *Adv. Mater.* **2024**, *36*, 11.
- [8] C. L. Li, X. Z. Jiang, H. L. Qi, D. P. Chen, T. C. You, S. Z. Huang, H. M. Yu, Y. Huang, M. J. Rao, G. H. Li, B. G. Xu, Y. J. Chen, L. B. Chen, *Energy Storage Mater.* **2025**, *75*, 11.
- [9] W. Liu, Q. W. Zhao, R. H. Jiang, X. Y. Ni, T. C. You, C. L. Li, Y. Z. Deng, B. A. Xu, Y. J. Chen, L. B. Chen, *Adv. Powder Mater.* **2025**, *4*, 10.
- [10] X. Y. Yuan, D. Zhang, H. F. Lu, C. X. Duan, Y. Jin, *IET Energy Syst. Integr.* **2024**, *22*.

- [11] L. Qian, W. T. Yao, R. Yao, Y. M. Sui, H. J. Zhu, F. C. Wang, J. W. Zhao, C. Y. Zhi, C. Yang, *Adv. Funct. Mater.* **2021**, *31*, 11.
- [12] J. Zeng, L. B. Dong, X. Guo, *Adv. Funct. Mater.* **2025**, *11*.
- [13] J. Zeng, H. Chen, L. B. Dong, X. Guo, *Adv. Funct. Mater.* **2024**, *34*, 10.
- [14] J. G. Ju, Y. Zhang, Y. X. Zhang, Z. H. Zhang, S. Chen, C. F. Zhao, W. M. Kang, *Chem. Eng. J.* **2024**, *481*, 9.
- [15] T. F. Li, S. X. Yan, H. Y. Dong, Y. Zheng, K. Ming, Y. Chen, H. T. Li, G. C. Li, Z. X. He, W. M. Li, Q. Wang, X. H. Song, J. F. Liu, E. H. Ang, Y. Wang, *J. Energy Chem.* **2024**, *97*, 1.
- [16] K. Zhang, S. Y. Xie, J. F. Liang, Z. Y. Zheng, Y. Li, L. B. Dong, *J. Membr. Sci.* **2025**, *722*, 8.
- [17] Z. Y. Zheng, D. Y. Ren, Y. Li, F. L. Kang, X. Li, X. Y. Peng, L. B. Dong, *Adv. Funct. Mater.* **2024**, *34*, 10.
- [18] M. C. Liu, C. Y. Tian, D. T. Zhang, Y. S. Zhang, B. M. Zhang, Y. Y. Wang, C. Y. Li, M. J. Liu, B. N. Gu, K. Zhao, L. B. Kong, Y. L. Chueh, *Nano Energy* **2022**, *103*, 11.
- [19] Q. Liu, Y. Wang, X. D. Hong, R. Zhou, Z. Hou, B. A. Zhang, *Adv. Energy Mater.* **2022**, *12*, 10.
- [20] Y. X. Li, H. F. Jia, U. Ali, H. Z. Wang, B. Q. Liu, L. Li, L. Y. Zhang, C. A. Wang, *Adv. Energy Mater.* **2023**, *13*, 12.
- [21] Y. Q. Zheng, P. X. Sun, X. Y. Zhang, N. W. Li, L. L. Wu, D. Y. Luan, X. T. Zhang, X. W. Lou, L. Yu, *Adv. Mater.* **2024**, *36*, 9.
- [22] L. Y. Wang, W. W. Huang, W. B. Guo, Z. H. Guo, C. Y. Chang, L. Gao, X. Pu, *Adv. Funct. Mater.* **2022**, *32*, 9.
- [23] Q. W. Zhao, W. Liu, Y. J. Chen, L. B. Chen, *Chem. Eng. J.* **2022**, *450*, 8.
- [24] W. L. Li, J. Zhang, Y. Wang, X. Y. Gu, G. S. Duan, Q. H. Zhang, Y. Hou, Z. J. Li, B. Yang, Z. Z. Ye, J. G. Lu, *Energy Storage Mater.* **2024**, *73*, 10.
- [25] X. Y. Zhang, Y. Xin, Q. Y. Shen, F. F. Wang, W. Xiao, *Ionics* **2023**, *29*, 5073.
- [26] H. Yu, Y. X. Zeng, N. W. Li, D. Y. Luan, L. Yu, X. W. Lou, *Sci. Adv.* **2022**, *8*, 9.
- [27] Y. T. Fang, P. C. Lei, H. R. Xing, K. L. Xu, M. G. Zhu, Z. C. Fan, K. W. Qi, Q. Y. Wu, Y. C. Zhu, *Energy Storage Mater.* **2022**, *53*, 13.
- [28] L. Wang, H. M. Yu, D. P. Chen, Y. L. Jin, L. L. Jiang, H. W. He, G. Zhou, Z. Q. Xie, Y. J. Chen, *Carbon Neutralization* **2024**, *3*, 996.
- [29] Q. W. Zhao, W. Liu, X. Y. Ni, H. M. Yu, C. X. Zhang, B. Wang, L. L. Jiang, H. W. He, Y. J. Chen, L. B. Chen, *Adv. Funct. Mater.* **2024**, *34*, 12.
- [30] J. L. Yang, P. H. Yang, W. Q. Yan, J. W. Zhao, H. J. Fan, *Energy Storage Mater.* **2022**, *51*, 259.
- [31] N. Hu, J. Tao, Y. Tan, H. W. Song, D. Huang, P. G. Liu, Z. J. Chen, X. C. Yin, J. L. Zhu, J. Xu, H. B. He, *Adv. Energy Mater.* **2024**, *14*, 13.
- [32] B. F. Cui, Y. Gao, X. P. Han, W. B. Hu, *J. Mater. Sci. Technol.* **2022**, *117*, 72.
- [33] J. L. Jiang, J. Lu, Y. H. Ou, G. F. Liu, S. Y. Lu, Y. Jiang, B. Zhao, J. J. Zhang, *ACS Appl. Mater. Interfaces* **2022**, *14*, 2930.
- [34] T. T. Wang, Y. A. Wang, X. M. Wang, M. W. Chang, Y. Zhang, J. H. You, F. Hu, K. Zhu, *Adv. Funct. Mater.* **2024**, *34*, 11.
- [35] M. M. Wang, W. P. Wang, Y. H. Meng, Y. Xu, J. F. Sun, Y. Yuan, M. Chuai, N. Chen, X. H. Zheng, R. H. Luo, K. Xu, W. Chen, *Energy Storage Mater.* **2023**, *56*, 424.
- [36] Z. X. Wu, Y. Wang, C. Y. Zhi, *Joule* **2024**, *8*, 2442.
- [37] S. D. Tan, Z. Y. Sang, Z. H. Yi, J. D. Guo, X. Q. Zhang, P. X. Li, W. P. Si, J. Liang, F. Hou, *EcoMat* **2023**, *5*, 13.
- [38] G. Kresse, J. Furthmüller, *Comput. Mater. Sci.* **1996**, *6*, 15.
- [39] M. Ernzerhof, J. P. Perdew, *J. Chem. Phys.* **1998**, *109*, 3313.

Manuscript received: March 20, 2025

Revised manuscript received: April 15, 2025

Version of record online: